Direct Z-scheme composite of CdS and oxygen-defected $CdWO_4$: An efficient visible-light-driven photocatalyst for hydrogen evolution

Xu Jia [a,b], Muhammad Tahir [a,b], Lun Pan [a,b], Zhen-Feng Huang [a,b], Xiangwen Zhang [a,b], Li Wang [a,b], Ji-Jun Zou [a,b,*]

[a] *Key Laboratory for Green Chemical Technology of the Ministry of Education, School of Chemical Engineering and Technology, Tianjin University, Tianjin 300072, China*
[b] *Collaborative Innovative Center of Chemical Science and Engineering (Tianjin), Tianjin 300072, China*

A B S T R A C T

Direct Z-scheme photocatalyst, which enables efficient charge separation and retains high redox ability, is promising material for visible-light-driven hydrogen evolution. Here we developed a one-step solvothermal method to fabricate direct Z-scheme $CdS/CdWO_4$ composite via treating $W_{18}O_{49}$ with CH_3CSNH_2 and $Cd(CH_3COO)_2$. By controlling the dosage of $Cd(CH_3COO)_2$, CdS nanoparticles decorated $CdWO_4$ nanowires (CS-2) is synthesized. UV–vis DRS and XPS spectra demonstrate that the $CdWO_4$ possesses a large amount of oxygen vacancies, which help to form ohmic contact and broaden light absorption. Compared with CdS, CS-2 Exhibits 18 times higher visible-light H_2 evolution activity using lactic acid as sacrificial agent and shows 7.8-fold higher photocurrent density. Moreover, photoelectrochemical test manifests the efficient separation of the photo-induced charge carriers. Radical-trapping experiments along with in-situ Pt photodeposition further prove that the charge transfer and separation follows Z-scheme mechanism. This work highlights the critical role of defects in the formation of direct Z-scheme composite.

© 2016 Elsevier B.V. All rights reserved.

1. Introduction

Photocatalytic hydrogen evolution is one of the most promising and eco-friendly solutions for clean energy production [1–4]. However, the development of effective and stable visible-light photocatalyst remains a great challenge. In the past few decades, various strategies have been proposed to design and fabricate highly efficient photocatalysts [5–7]. Among them, the combination of different semiconductors into composites can take full advantage of each component and is in favour of photocatalytic hydrogen evolution. Type II heterojunction is the most common composite in which both conduction band and valence band of one semiconductor are either higher or lower than the other [8–10]. The staggered band alignment formed on the interface can drive photo-induced electrons to the semiconductor with lower conduction band potential and holes to the one with higher valence band potential, respectively. As a result, the spatial separation of charge

carriers is achieved, and the recombination of charges that is the main factor limiting the photocatalytic performance is alleviated to some degree. However, this improvement on charge separation is at the cost of weakening the redox ability, because the photo-induced electrons and holes are concentrated on the band with lower redox potentials. This is not favourable for the photocatalytic process requiring high redox ability, especially for H_2 production.

Z-scheme photocatalytic system has been designed to solve the problem of Type II heterojunction [11,12]. Actually, it has the same band alignment with Type II heterojunction, but exhibits an opposite direction of charge transfer. The photo-induced electrons on the semiconductor with lower conduction band potential will combine with the holes on another semiconductor with higher valence band potential, and the electrons and holes with stronger redox ability remain on two semiconductors. In that way, the Z-scheme system can achieve efficient charge separation and strong redox ability simultaneously. Typical Z-scheme system is composed by two individual photocatalysts and using electron shuttles (IO_3^-/I^- or Fe^{3+}/Fe^{2+}) as redox mediators, but it is complicated and suffers from various backward reaction between redox mediators and photocatalysts. Recently, the redox-mediator-free Z-scheme system attracts increasingly interest. It is worth noting that the ohmic

contact between two semiconductors is indispensable and the presence of metal conductors between two semiconductors such as Au and Pt could help the formation of ohmic contact [12–14]. Although the metal conductors generally show stronger ability for charge transfer due to the lower electrical resistance, the direct Z-scheme without conductors is more cost-effective. Therefore, optimizing the contact interface is of great significance.

Recently, oxygen-defected semiconductors are attracting intensive interest as visible-light-active photocatalyst [15–17]. The introduction of oxygen vacancies can create defect levels between the valence and conduction band, which induces new channels for light absorption and thus improves solar harvesting [16–19]. Furthermore, it is believed that abundant defects aggregating at the contact interface of composites is beneficial to the formation of ohmic contact, because the interfacial defects can act as the centers for charge recombination [12,20]. Thus, the introduction of oxygen vacancies may also contribute to the construction of direct Z-scheme.

CdS is regarded as one of the most promising material for solar-driven hydrogen evolution due to the optimal band gap and suitable conduction band level [21,22]. However, its activity and stability are far from satisfactory because of the rapid charge recombination and photo corrosion [22,23]. Combining CdS with other semiconductors is an effective way to solve this problem [24,25]. For example, $CdS/CdWO_4$ composite can form Type II heterojunction and inhibits the electron-hole recombination [26,27]. However, the $CdWO_4$ produced is defect-free and the bandgap is very large ($\sim$3.8 eV) that limits the light harvesting and hinders photocatalytic application [26–29]. In $CdWO_4$ crystal, W^{6+} and Cd^{2+} ions both have octahedral oxygen coordination and each octahedron shares two corners with its neighbors [28–30]. The existence of WO_6 octahedra indicates the feasibility of oxygen vacancy introduction, as broadly studied in tungsten oxides [31,32]. So the light absorption of the composite can be further improved via defect engineering and the defects on the contact interface may help to form ohmic contact, thus favors the construction of direct Z-scheme.

In this work, we develop a novel method to synthesis CdS decorated oxygen-defected $CdWO_4$ nanowires using $W_{18}O_{49}$ as precursor. Benefited from the reductive environment of synthetic solution, the oxygen vacancies in $W_{18}O_{49}$ precursor are well retained and the as-synthesized composite possesses a well-built contact interface that facilitates the formation of ohmic contact. Meanwhile, the oxygen-defected $CdWO_4$ in composite greatly promotes the visible light harvesting ability. As a result, the composite exhibits remarkably enhanced visible-light-driven hydrogen evolution activity, and, contrary to the reported type II $CdS/CdWO_4$ junction, shows a Z-scheme pathway for charge transfer. This work highlights the role of defects in the direct Z-scheme composite and provides a facile way for the design of direct Z-scheme interface.

2. Experimental

2.1. Materials

WCl_6, $Cd(CH_3COO)_2 \cdot 2H_2O$ and Rhodamine B (RhB) were obtained from J&K Chemical Co. CH_3CSNH_2, n-Propanol, ethanol, lactic acid, ammonium oxalate, isopropyl alcohol, 1,4-benzoquinone, ammonium acetate and hydrogen peroxide (30 wt.% aqueous solution) were purchased from Tianjin Guangfu Fine Chemical Research Institute. All the chemicals were of reagent grade and used as received.

2.2. Synthesis of photocatalysts

Spindle-like $W_{18}O_{49}$ was prepared by alcoholysis of WCl_6 according to literature [33] and was used as precursor. Typically, 0.297 g WCl_6 was dissolved in 50 mL n-Propanol, transferred to a Teflon-lined autoclave (100 mL) and heated at 200 °C for 24 h. The produced $W_{18}O_{49}$ was collected via centrifugation, washed thoroughly with ethanol and dispersed in 40 mL ethanol with sonication. 1.77 mmol CH_3CSNH_2 was added in the above solution and stirred for 1 h, then a 40 mL ethanol solution of $Cd(CH_3COO)_2 \cdot 2H_2O$ was added dropwise and stirred for another 1 h. The mixture (with 80 mL total volume) was solvothermally treated in a 100 mL Teflon-lined autoclave at 150 °C for 12 h. Finally the product was centrifuged, washed with ethanol and dried at 40 °C overnight. With the increase of Cd dosage, the molar ratio of $Cd(CH_3COO)_2$ to CH_3CSNH_2 was fixed as 1, 1.5, 2 and obtained products were named as CS-1, CS-1.5, CS-2, respectively.

CdS was synthesized similar to CS-1 but without adding $W_{18}O_{49}$. CS-2H was synthesized similar to CS-2, except $W_{18}O_{49}$ were pretreated by 50 mL H_2O_2 (30 wt.%) to remove some oxygen vacancies. The preparation of $CdWO_4$ was similar to CS-2 by replacing CH_3CSNH_2 with CH_3COONH_4 and the as-synthesized $CdWO_4$ was treated with hydrogen at 500 °C for 2 h to obtain oxygen-defected $CdWO_4$.

2.3. Characterizations

Crystal structures were recorded using a Rigaku D/max-2500 X-ray diffractometer (XRD) equipped with a Cu Kα irradiation source. Morphology and microstructure were examined on a Tecnai G^2 F-20 transmission electron microscope (TEM). Energy dispersive spectrum (EDS) characterization was performed with an EDX system attached to TEM. UV–vis diffuse reflectance spectra (UV–vis DRS) were recorded with a Hitachi U-3010 spectrometer equipped with a 60 mm diameter integrating sphere using $BaSO_4$ as the standard reflectance. The surface composition and chemical states were analyzed using a PHI-1600 X-ray photoelectron spectroscope (XPS) equipped with Al Ka radiation, and the binding energy was calibrated using the C1s peak (284.6 eV) of the contaminated carbon.

2.4. Photocatalytic hydrogen evolution

The photocatalytic activity was evaluated with 20 mg photocatalyst suspended in 100 mL aqueous solution containing 10 vol.% of lactic acid as the sacrificial agent. The suspension was sealed in a quartz vessel, sonicated for 10 min and purged with argon gas for 30 min to remove all air in solution and headspace. After degassing, the vessel was vertically irradiated by a 300 W Xe lamp (PLS-SXE 300/300UV, Beijing Perfectlight Technology Co. Ltd.) coupled with a UV cutoff filter (>420 nm). The irradiation area was ca. 20 cm^2, the light density was 23 mW/cm^2 at 420 nm as measured with a radiometer (Photoelectric Instrument Factory, Beijing Normal University, Model UV-A). The temperature of reaction solution was maintained at 0 °C. Cocatalysts (0.5 wt.% Pt) were introduced by in-situ photodeposition using H_2PtCl_6 as precursor [34,35]. The amount of generated H_2 was analyzed by a gas chromatograph (Bruker 450-GC) with a thermal conductivity detector (TCD, molecular sieve 5A, argon carrier gas 99.999%).

2.5. Photoelectrochemical measurements

Photoelectrochemical measurements were performed on Ivium CompactStat.e20250 workstation using a three-electrode cell with a working electrode, a Pt counter electrode, and an Ag/AgCl reference electrode. Na_2SO_4 (0.2 M) was used as the electrolyte solution and lactic acid (10 vol.%) was served as the hole scavenger. The
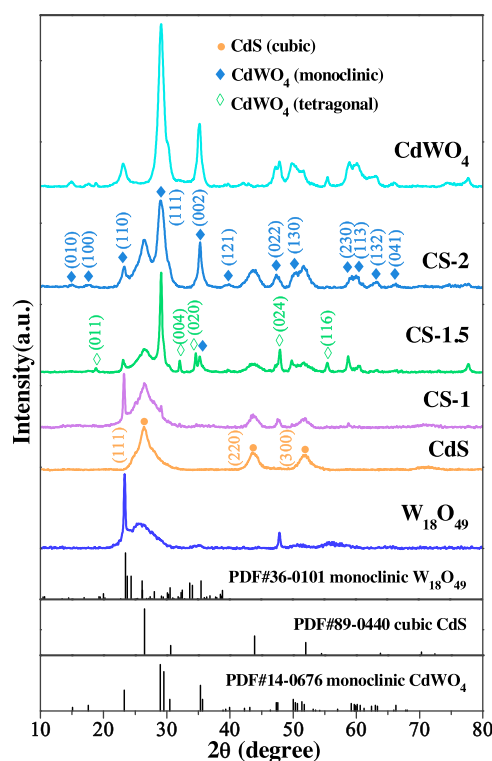
Fig. 1. XRD patterns of CS-Series, CdS, $W_{18}O_{49}$ and $CdWO_4$.

Table 1
Phase composition, crystalline size and bandgap of synthesized samples.

samples	phase composition	crystalline size (nm)	bandgap (eV)
$W_{18}O_{49}$	monoclinic $W_{18}O_{49}$	17.47	2.53
CdS	cubic CdS	9.09	2.23
CS-1	monoclinic $W_{18}O_{49}$ cubic CdS	17.98 9.37	2.22
CS-1.5	monoclinic $CdWO_4$ tetragonal $CdWO_4$ cubic CdS	13.48 21.03 8.96	2.47
CS-2	monoclinic $CdWO_4$ cubic CdS	10.80 9.18	2.41
$CdWO_4$	monoclinic $CdWO_4$	10.50	3.74
CS-2H	–	–	2.41
$dCdWO_4$	–	–	3.64

working electrode was prepared by spin-coating a photocatalyst slurry on an F-doped tin oxide (FTO) glass electrode (2.5×2.5 cm²) and subsequently vacuum drying at 40 °C overnight. The thickness of all investigated working electrodes are same. All the potentials were obtained with reference to the Ag/AgCl. Electrochemical impedance spectroscopy (EIS) measurements were carried out with a sinusoidal ac perturbation of 10 mV applied to the electrodes over a frequency range of $0.01–10^5$ Hz.

2.6. Radical-trapping experiments

The photo-degradation of RhB was conducted in aqueous solution under UV–vis light irradiation. The reactor was open to air in order to reach the air-equilibrated condition. Typically, 20 mg of photocatalyst were dispersed in 100 mL RhB (0.01 mM) solution with magnetic stirring. Prior to the irradiation, the suspension was stirred for 20 min in the dark to ensure the adsorption equilibrium. The reaction temperature was controlled at 25 °C. Radical scavengers including ammonium oxalate (AO, 6 mM), isopropyl alcohol (IPA, 10 mM) and 1,4-benzoquinone (BQ, 0.1 mM) were added to scavenge the h^+, $\bullet OH$ and $\bullet O_2^-$ species, respectively. During the reaction, samples were withdrawn at intervals, centrifuged, and analyzed. The concentration of residual was determined using a Hitachi U-3010 UV–vis spectrometer by monitoring the characteristic absorption wavelength of 553 nm for RhB. The data were fitted using a pseudo-first-order kinetic equation to obtain the reaction rate constant (k).

3. Results and discussion

3.1. Structure of photocatalysts

XRD investigation was performed to explore the crystal structure and phase of as-synthesized materials (Fig. 1). The composition of as-synthesized CS-Series products changes dramatically with the increase of Cd dosage. CS-1 is a composite of monoclinic $W_{18}O_{49}$

(JCPDS No. 36-0101) and cubic CdS (JCPDS No. 89-0440). Whereas CS-1.5 is a ternary mixture of monoclinic $CdWO_4$ (JCPDS No. 14-0676), tetragonal $CdWO_4$ [28,36] and CdS. As for CS-2, it is mainly composed of CdS and pure monoclinic phase $CdWO_4$. The phase composition of these samples and corresponding average crystalline size calculated by Scherrer equation were listed in Table 1.

The morphology of the products were characterized using transmission electron microscope (TEM). $W_{18}O_{49}$ exhibits a spindle-like morphology with a diameter of 150 nm and a length of 500 nm (Fig. 2a), whereas CdS is cluster made of tiny nanoparticles of ca. 10 nm (Fig. 2b). Fig. 2c shows that CS-1 is spindle-like particles decorated by tiny nanoparticles on the surface. According to the HRTEM (Fig. 2d), the spindle-like particles and tiny nanoparticles can be assigned to $W_{18}O_{49}$ and CdS, respectively. CS-1.5 is stacked mixtures of cube-like particles (ca. 100 nm in side length) and nanowires (ca. 10–20 nm in diameter and 300 nm in length) decorated with CdS nanoparticles (Fig. 2e,f). The fringe spacing of tetragonal $CdWO_4$ is identified to the cube-like particle (Fig. 2f), which corresponds to the diffraction peak at 18.8° (the [011] facets) in XRD pattern [36]. As for CS-2, a network structure assembled by nanowires (ca. 10–20 nm in diameter and 200–500 nm in length) is formed and tiny nanoparticles are deposited on the nanowires (Fig. 2g, h). HRTEM image (Fig. 2h) shows that the nanowires are monoclinic $CdWO_4$ and the tiny particles around the nanowires are cubic CdS. This results match well with the XRD characterization and confirm that the composites possess well-built contact interfaces.

Fig. 3a shows the optical absorption of CdS, CS-Series and $CdWO_4$. CdS shows a strong and broad absorbance in the visible region due to its narrow bandgap, while the optical absorption of $CdWO_4$ is quite limited due to the wide bandgap. $W_{18}O_{49}$ exhibits a very wide absorption tail in visible light owing to the existence of oxygen vacancies [17,33]. CS-1 shows an absorption feature mixed by $W_{18}O_{49}$ and CdS. As for CS-1.5 and CS-2, an obvious absorption tail can be observed in the visible and near infrared region, which is quite different from $CdWO_4$ and CdS. While this feature is very similar to $W_{18}O_{49}$ and indicates the existence of oxygen vacancies in $CdWO_4$ of CS-1.5 and CS-2. H_2-treatment at high temperature is an effective way to produce oxygen vacancies [18,37], so pure $CdWO_4$ was treated in H_2 at 500 °C. As expected, the obtained sample ($dCdWO_4$) also exhibits a strong absorption tail till the near infrared region. This result further confirms the oxygen-deficient feature of the $CdWO_4$ in CS-1.5 and CS-2. Compared to the previously reported $CdS/CdWO_4$ composite [26,27], the visible light absorption of composite is greatly promoted due to the existence of oxygen vacancies.
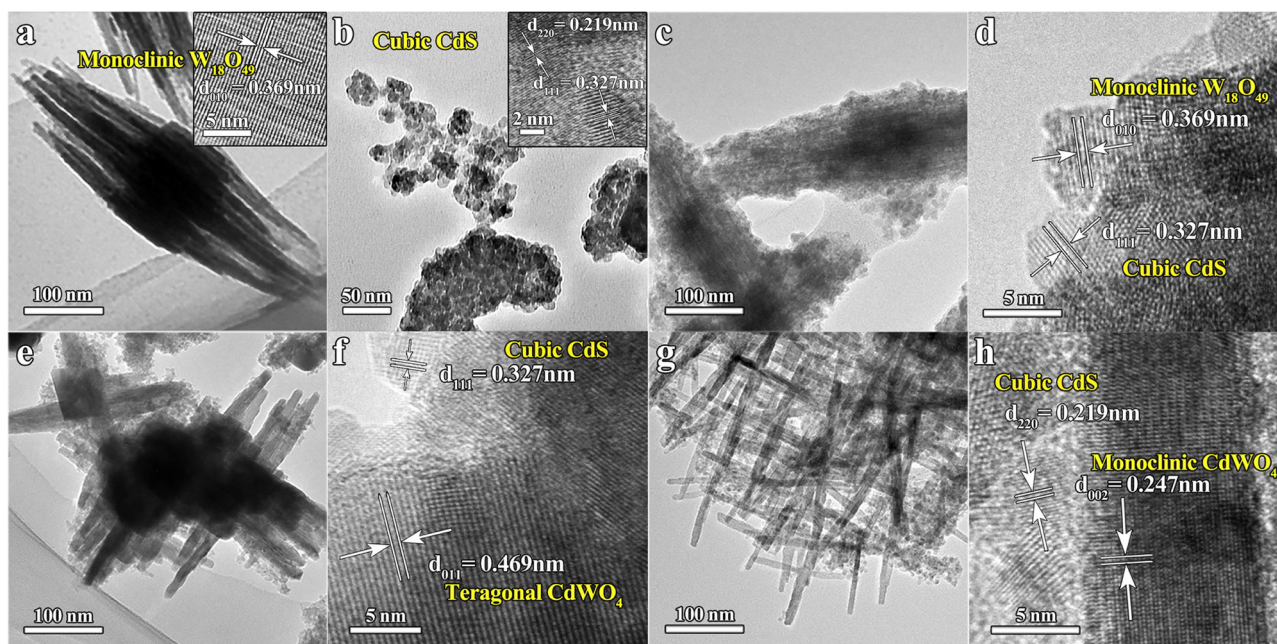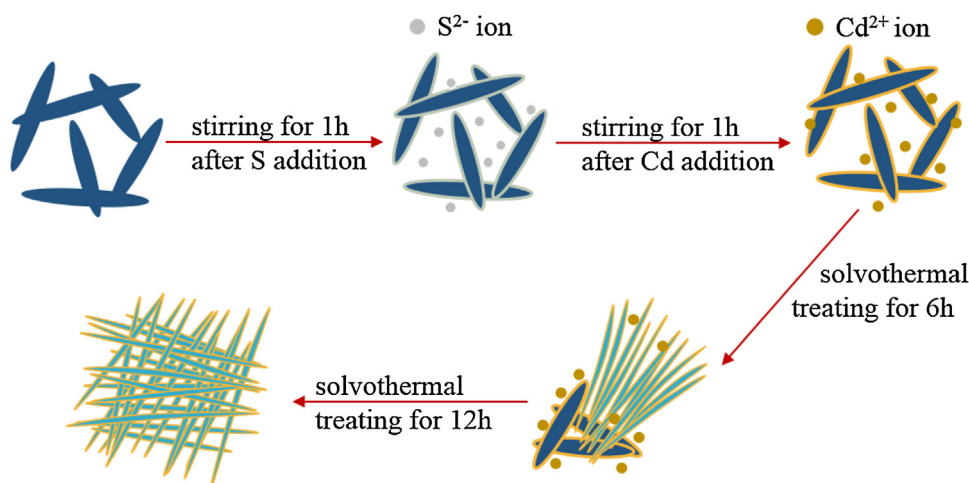
Fig. 2. TEM images of (a) $W_{18}O_{49}$, (b) CdS, (c, d) CS-1, (e, f) CS-1.5, (g, h) CS-2.

Scheme 1. Schematic illustration of formation mechanism of CS-2.

In addition, the bandgap of the synthesized materials was estimated from UV–vis DRS spectra using the Kubelka-Munk function (Eq. (1)).

$$\alpha h\nu = A\left(h\nu - E_g\right)^{n/2} \tag{1}$$

where $h\nu$, α, A, and E_g are light energy, absorption index, constant value, and bandgap energy of semiconductor, respectively. The coefficient n relies on the transition type of semiconductor, being 1 for CdS and CS-Series and 4 for $W_{18}O_{49}$, $CdWO_4$ and $dCdWO_4$ [38–40]. The Kubelka−Munk function transformed differential spectra are shown in Fig. 3b,c and the bandgap of samples is listed in Table 1. With the increase of Cd dosage, the bandgap of CS-Series increase at first and then decreases. The bandgap of CS-1.5 is larger than CS-1 and CS-2 due to the formation of wide-bandgap tetragonal $CdWO_4$ compared with monoclinic phase.

X-ray photoelectron spectroscopy (XPS) was employed to analyze the oxidation state of W element in $CdWO_4$. As shown in Fig. 4a, the W_{4f} spectra of CS-2 can be divided into four peaks. The strong peaks at 35.4 and 37.6 eV correspond to W^{6+}, while the weak peaks

at 34.5 and 36.7 eV correspond to W^{5+} [41]. Similarly, the W_{4f} spectra of $dCdWO_4$ (Fig. 4b) can also be divided into multiple peaks referred to W^{6+} and W^{5+}. However, pure $CdWO_4$ (Fig. 4c) only shows two sharp peaks of W_{4f}, which is a typical feature for W^{6+}. The presence of W^{5+} signals clearly confirm the existence of oxygen vacancies in $CdWO_4$ of CS-2.
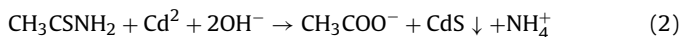
3.2. Formation mechanism of oxygen-defected $CdWO_4$ in CS-2

To investigate the synthetic mechanism of CS-2, TEM images and XRD patterns (Fig. S1) were recorded on every stage of the synthetic process of CS-2, as illustrated in Scheme 1. Firstly, dissolved CH_3CSNH_2 is absorbed on the spindle-like $W_{18}O_{49}$. After the addition of $Cd(CH_3COO)_2$, absorbed CH_3CSNH_2 is hydrolyzed and releases S^{2-} due to the weak alkaline environment provided by the hydrolysis of acetate. Then, CdS particles are precipitated by reaction of Cd^{2+} with S^{2-} on the surface of $W_{18}O_{49}$ along with
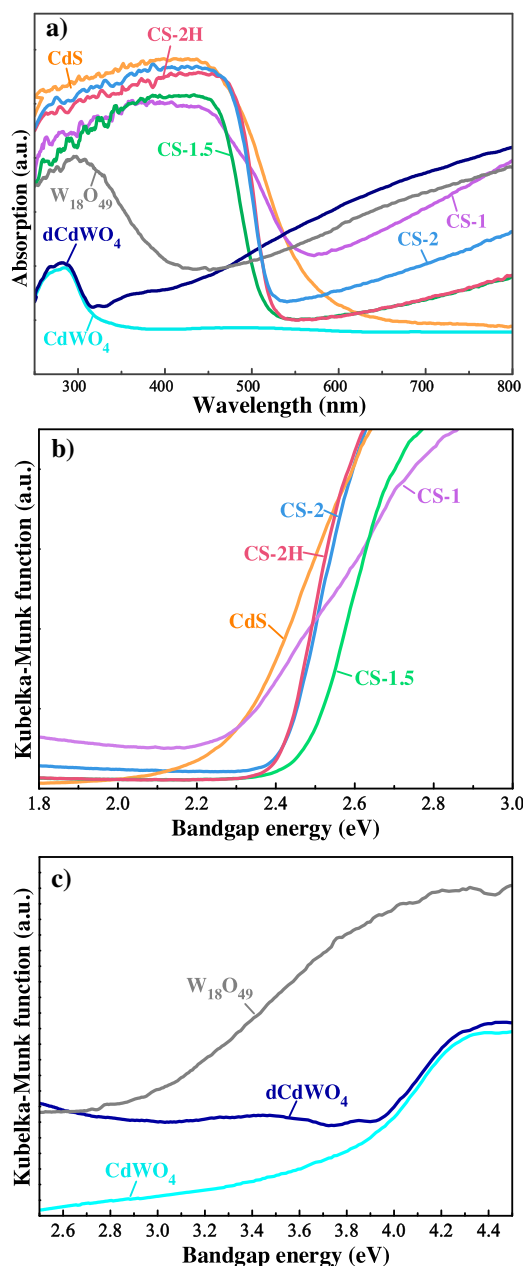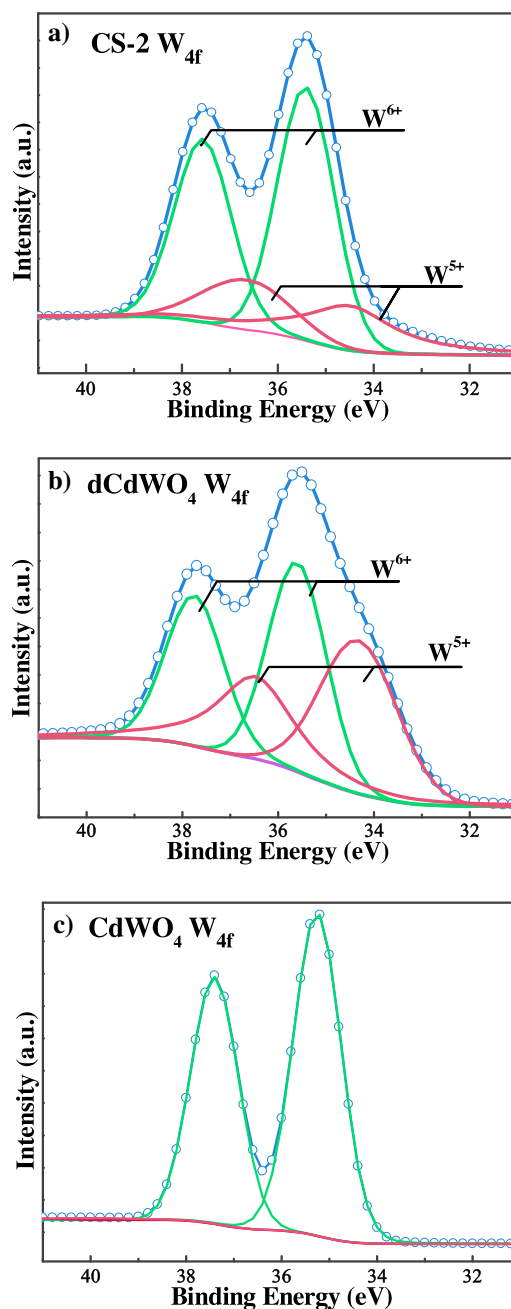
Fig. 3. a) UV–vis DRS spectra of CS-Series, CdS, $W_{18}O_{49}$, $CdWO_4$ and $dCdWO_4$; Kubelka−Munk function transformed differential spectra of b) CS-Series, CdS, c) $W_{18}O_{49}$, $CdWO_4$ and $dCdWO_4$.

Fig. 4. Devolution of W_{4f} XPS spectra of (a) CS-2, (b) $dCdWO_4$ and (c) $CdWO_4$.

NH_4^+ and CH_3COO^- (Eq. (2)). During the solvothermal treatment, $W_{18}O_{49}$ and the Cd residues are converted to $CdWO_4$ nanowires.

$$CH_3CSNH_2 + Cd^2 + 2OH^- \rightarrow CH_3COO^- + CdS \downarrow + NH_4^+ \qquad (2)$$

However, simply solvothermally treating $W_{18}O_{49}$ with $Cd(CH_3COO)_2$ produces $CdWO_4$ and large amount of CdO (Fig. S2a). Therefore, the presence of NH_4^+ and CH_3COO^-, produced by reaction between CH_3CSNH_2 and Cd^{2+}, may play a vital role to prevent the formation of CdO. To verify this, CH_3COONH_4, $W_{18}O_{49}$ and $Cd(CH_3COO)_2$ were treated under the same conditions. This time, pure $CdWO_4$ with phase structure and morphology identical to $CdWO_4$ in CS-2 is obtained, as shown by the XRD pattern and TEM image (Fig. S2). However, UV–vis DRS and XPS characterizations (Figs. 3 a and 4) show the as-synthesized $CdWO_4$ does not have any oxygen vacancies, which is quite different from the CS-Series. It is possible that, in the absence of CH_3CSNH_2, the solution cannot

maintain a reductive environment to prevent the elimination of oxygen vacancies.

3.3. Photocatalytic activity

The photocatalytic hydrogen evolution performances were evaluated under visible light irradiation (Fig. 5a). Pure CdS shows very low activity (0.51 mmol h^{-1} g^{-1}) due to rapid recombination of photo-induced charge carriers, $W_{18}O_{49}$, $CdWO_4$ and oxygen-defected $CdWO_4$ are almost inactive. In contrast, CS-1.5 and CS-2 display enhanced photocatalytic performance. The highest H_2 evolution rate of 9.17 mmol $h^{-1} \cdot g^{-1}$ is achieved on CS-2, which surpasses that of CdS by nearly 18 times. After 0.5 wt.% Pt is in-situ deposited on the surface, the H_2 evolution rates are further increased. The composite of CdS and oxygen-defected $CdWO_4$ undoubtedly shows superior activity compared to $CdS/CdWO_4$
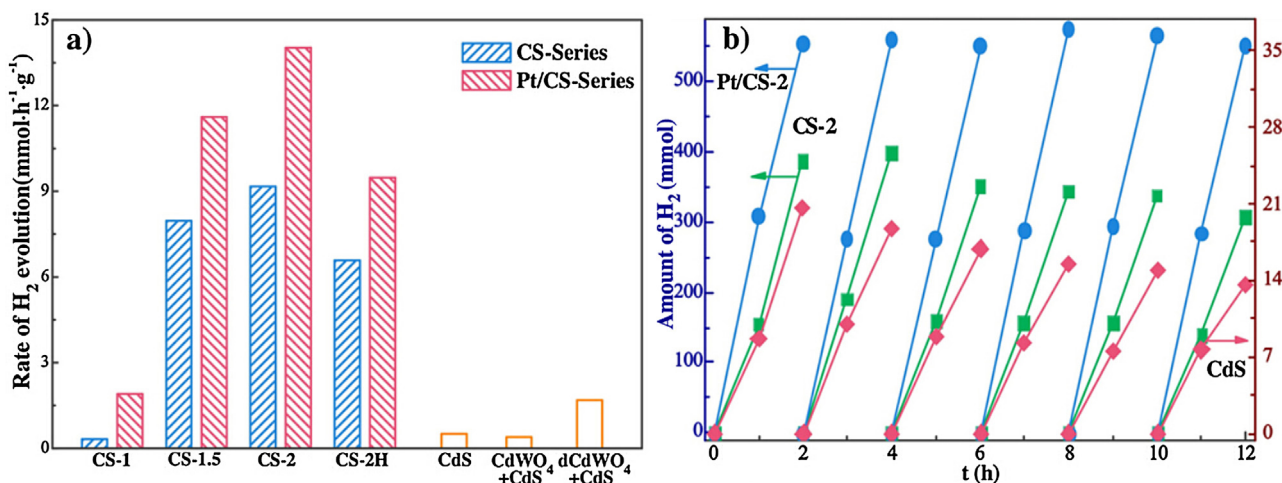
Fig. 5. (a) H_2 evolution rate of synthesized photocatalysts, (b) stability of CS-2 and CdS.

composite [26,27]. Moreover, this present composite is more active than the S-doped C_3N_4/Au/CdS in which Au is used as electron mediator to construct Z-scheme and the activity is increased 4.2 times compared to pure CdS [42].

To test the stability of CS-2, six consecutive reactions were carried out (Fig. 5b). The amount of H_2 keeps increasing steadily in each cycle. Although the activity of CS-2 is in decline during long period irradiation, about 80% of activity still remains after 6 cycles. But pure CdS retains only 66% of activity under the same reaction condition, the gradual regression of activity mainly arises from the photocorrosion of CdS by photo-generated holes, a major problem for metal sulfide photocatalysts [23]. While CS-2 shows superior stability due to the more efficient charge separation and consumption of photo-generated holes in CdS. Besides, after Pt deposition, CS-2 shows a quite stable H_2 evolution rate within 12 h.

It is noted that the physical mixture of $CdWO_4$ nanowires and CdS nanoparticles shows no improvement on photocatalytic H_2 generation, whereas the mixture of defected $CdWO_4$ and CdS shows nearly 3-fold improvement compared with pure CdS. This result clearly demonstrates that the synergic effect of composite is caused by oxygen vacancies. And for CS-2, this effect is more significant attributed to the well-built interface between CdS and defected $CdWO_4$. To study the role of defects, the oxygen vacancies of CS-2 are reduced by treating the $W_{18}O_{49}$ precursor with hydrogen peroxide beforehand and the as-synthesized sample is CS-2H. Although it has the same morphology and crystalline phase as CS-2 (Fig. S3), the activity of CS–2H is reduced to 6.59 mmol h^{-1} g^{-1} due to the decrease of oxygen vacancies. Therefore, it can be concluded that the oxygen vacancies in $CdWO_4$ play a key role on the enhancement of photocatalytic performance.

Photoelectrochemical measurements were also performed in order to further illustrate the ability of photo-induced charge separation. As shown in Fig. 6a, chopped photocurrent–time curves are presented for each light on and off event in multiple 60 s on-off cycles. The composites show intensified photocurrent density owing to the junction-promoted efficient charge separation and enhanced light absorption. The photocurrent density of CS-2 electrode is about 7.8-fold higher than that of pure CdS electrode. Additionally, from EIS Nyquist plot (Fig. 6b), decreased radius of semicircular on composites is observed, which further confirms the effective separation of the photo-induced charge carriers and fast interfacial charge transfer.

3.4. Z-scheme mechanism

As shown in Table 1, the bandgaps of CdS and $CdWO_4$ are 2.23 and 3.74 eV, respectively. The band structures of CdS and $CdWO_4$ can be further calculated using the following equations: (Eqs. (3) and (4))

$$E_{VB} = \chi - E^e + 0.5E_g \tag{3}$$

$$E_{CB} = E_{VB} - E_g \tag{4}$$

where E_{VB} and E_{CB} are the valence and conduction band potentials, respectively, E^e is the energy of free electrons on the hydrogen scale (4.5 eV vs. NHE), and χ is the electronegativity for a semiconductor which is defined as the geometric mean of the absolute electronegativity of the constituent atoms in the semiconductor, being 5.19 and 6.28 eV for CdS and $CdWO_4$, respectively. The calculated E_{VB} and E_{CB} of CdS are +1.80 and −0.43 eV, while the E_{VB} and E_{CB} of $CdWO_4$ are +3.65 and −0.09 eV, respectively. For defected $CdWO_4$, the existence of oxygen vacancies may create defect levels under the conduction band and the increased visible light absorption could be attributed to the electron excited from valence band to defect levels or from defect levels to the conduction band [16,18].

Previous literatures report that coupling CdS with $CdWO_4$ forms a Type II heterojunction [26,27]. In this case, photo-induced electrons in the CB (conduction band) of CdS transfer to $CdWO_4$, while photo-induced holes in the VB (valence band) of $CdWO_4$ transfer to CdS (See Scheme 2). However, the conduction band (CB) of $CdWO_4$ is very close to the potential of water reduction, and it is hard for the excited electrons to drive the hydrogen evolution reaction. Actually, experiments show that $CdWO_4$ and defected $CdWO_4$ are inactive, even after loading Pt cocatalyst. So the active site of hydrogen evolution in CS-2 composite should be CdS and the charge transfer must follow the Z-scheme mechanism.

To demonstrate the pathway for charge transfer, radical-trapping experiments (Fig. 7a) of RhB photo-degradation was conducted over CdS and CS-2. The scavengers ammonium oxalate (AO), isopropyl alcohol (IPA), and 1,4-benzoquinone (BQ) were used to quench the holes (h^+), hydroxyl radicals (•OH) and superoxide radicals (•O_2^-), respectively. Limited by the oxidizing ability of valence band, CdS cannot produce ·OH and the major active species are the holes and •O_2^- (reduced by electrons). As a result, the degradation rate is almost unchanged when IPA is added, whereas the degradation rate is dramatically decreased to 33% and 11% when
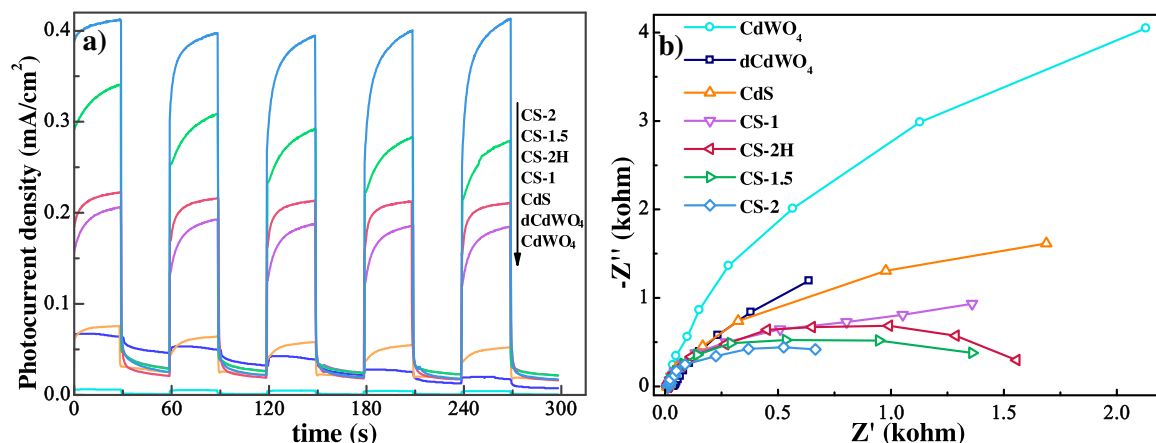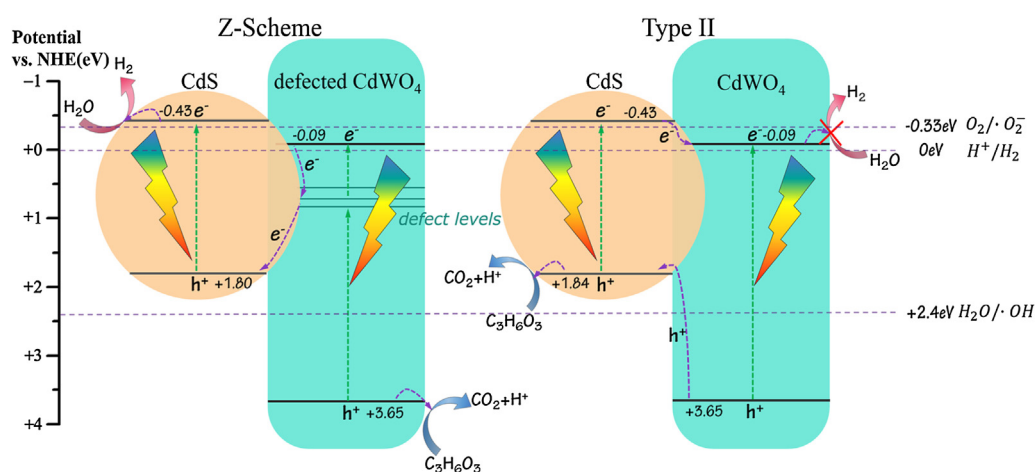
Fig. 6. (a) Transient photocurrent density versus time plots at 0.8 V and (b) the corresponding EIS Nyquist plot.

Scheme 2. Z-scheme and Type II heterojunction charge transfer mechanisms over CdS/CdWO$_4$.
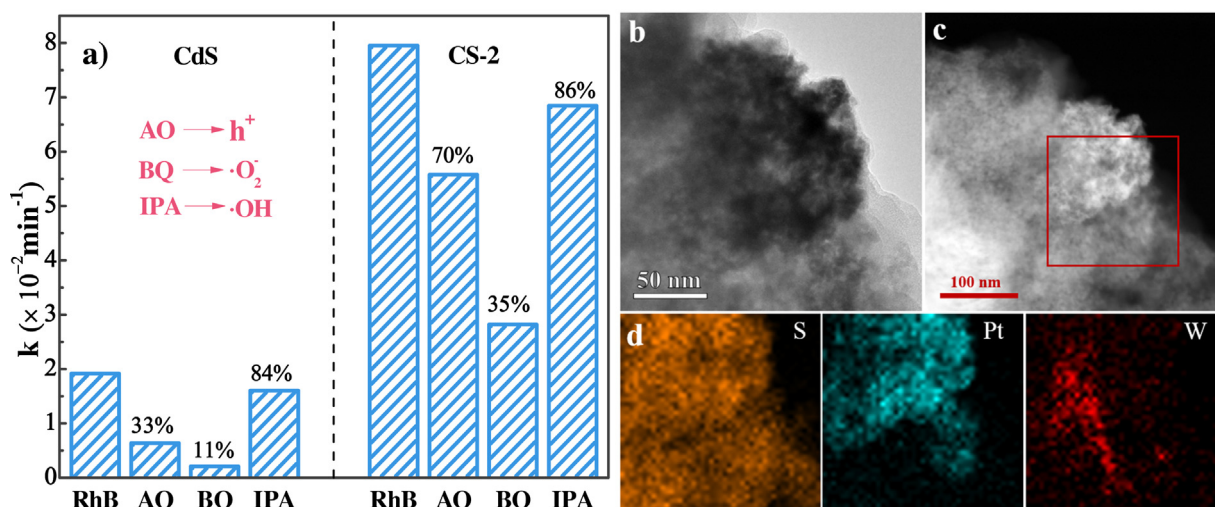

Fig. 7. (a) Effect of scavengers on RhB photo-degradation under visible light; (b) TEM and (c) HAADF−STEM image of in-situ photodeposited Pt on CS-2; (d) EDX mapping images of S, Pt, and W element.

$\cdot O_2^-$ and h$^+$ are quenched by BQ and AO, respectively. Similarly, the activity of CS-2 shows considerable decline after BQ was added (35% of activity remains), suggesting $\cdot O_2^-$ is still the major active species in photocatalysis. Since the potential level of CdWO$_4$ is too low to produces $\cdot O_2^-$, electrons photo-induced in CS-2 must locate

on CdS instead of CdWO$_4$. This charge transfer is contrary to that of Type II heterojunction and must follows the Z-Scheme mechanism. Furthermore, TEM and EDX mapping of Pt/CS-2 (Fig. 7b), where Pt is photo-deposited to probe the active sites, show that Pt is selectively deposited on CdS nanoparticles attached to CdWO$_4$

(a rod-like particle identified in EDX mapping of W element). This confirms that the electron is located on CdS to serve as active sites for hydrogen evolution.

Scheme 2 schematically illustrates the Z-scheme mechanism between oxygen-defected $CdWO_4$ and CdS. The oxygen defects located at the $CdS/CdWO_4$ interface can form quasi-continuous energy levels, which induce the formation of ohmic contact and lower the interfacial electric resistance. The photo-induced electrons in the CB of $CdWO_4$ will recombine with the holes in the VB of CdS through the ohmic contact. As a consequence, the electrons and holes in the CB of CdS and the VB of $CdWO_4$ are well isolated. Thus, photo-generated electrons in CdS are available to drive the hydrogen evolution.

4. Conclusions

We successfully fabricated CdS nanoparticles decorated oxygen-defected $CdWO_4$ nanowires. Benefited from Ohmic contact induced by oxygen defects, the interfacial charge transfer is changed from conventional type II heterojunction to direct Z-scheme. This structure improves not only the charge separation but also retains the strong reductive capability of CdS. As a result, this photocatalyst exhibits remarkably higher hydrogen evolution activity and stability under visible light, compared with pure CdS. In particularly, the H_2 evolution rate introduction of CS-2 is 18 times higher than that of CdS. This work suggests that defect engineering may help to design Z-scheme interface for hydrogen evolution.

Acknowledgments

Appendix A. Supplementary data

Supplementary data associated with this article can be found, in the online version, at http://dx.doi.org/10.1016/j.apcatb.2016.05.046.

References

[1] Z.-F. Huang, J. Song, K. Li, M. Tahir, Y.-T. Wang, L. Pan, L. Wang, X. Zhang, J.-J. Zou, J. Am. Chem. Soc. 138 (2016) 1359–1365.
[2] Z.-F. Huang, J. Song, L. Pan, Z. Wang, X. Zhang, J.-J. Zou, W. Mi, X. Zhang, L. Wang, Nano Energy 12 (2015) 646–656.
[3] X. Li, J. Yu, J. Low, Y. Fang, J. Xiao, X. Chen, J. Mater. Chem. A 3 (2015) 2485–2534.
[4] T. Hisatomi, J. Kubota, K. Domen, Chem. Soc. Rev. 43 (2014) 7520–7535.
[5] H. Yu, R. Liu, X. Wang, P. Wang, J. Yu, Appl. Catal. B: Environ. 111–112 (2012) 326–333.
[6] X. Wang, S. Li, Y. Ma, H. Yu, J. Yu, J. Phys. Chem. C 115 (2011) 14648–14655.
[7] L. Pan, J.-J. Zou, S. Wang, Z.-F. Huang, A. Yu, L. Wang, X. Zhang, Chem. Commun. 49 (2013) 6593–6595.
[8] Y.-P. Yuan, L.-W. Ruan, J. Barber, S.C.J. Loo, C. Xue, Energy Environ. Sci. 7 (2014) 3934–3951.
[9] Z.-F. Huang, J.-J. Zou, L. Pan, S. Wang, X. Zhang, L. Wang, Appl. Catal. B: Environ. 147 (2014) 167–174.
[10] Z.-F. Huang, J. Song, L. Pan, X. Jia, Z. Li, J.-J. Zou, X. Zhang, L. Wang, Nanoscale 6 (2014) 8865–8872.
[11] K. Maeda, ACS Catal. 3 (2013) 1486–1503.
[12] P. Zhou, J. Yu, M. Jaroniec, Adv. Mater. 26 (2014) 4920–4935.
[13] H. Tada, T. Mitsui, T. Kiyonaga, T. Akita, K. Tanaka, Nat. Mater. 5 (2006) 782–786.
[14] L.J. Zhang, S. Li, B.K. Liu, D.J. Wang, T.F. Xie, ACS Catal. 4 (2014) 3724–3729.
[15] N. Liu, V. Häublein, X. Zhou, U. Venkatesan, M. Hartmann, M. Mačković, T. Nakajima, E. Spiecker, A. Osvet, L. Frey, P. Schmuki, Nano Lett. 15 (2015) 6815–6820.
[16] F. Lei, Y. Sun, K. Liu, S. Gao, L. Liang, B. Pan, Y. Xie, J. Am. Chem. Soc. 136 (2014) 6826–6829.
[17] G. Xi, S. Ouyang, P. Li, J. Ye, Q. Ma, N. Su, H. Bai, C. Wang, Angew. Chem. Int. Ed. 51 (2012) 2395–2399.
[18] J. Yan, T. Wang, G. Wu, W. Dai, N. Guan, L. Li, J. Gong, Adv. Mater. 27 (2015) 1580–1586.
[19] A. Naldoni, M. Allieta, S. Santangelo, M. Marelli, F. Fabbri, S. Cappelli, C.L. Bianchi, R. Psaro, V.D. Santo, J. Am. Chem. Soc. 134 (2012) 7600–7603.
[20] S. Bai, J. Jiang, Q. Zhang, Y. Xiong, Chem. Soc. Rev. 44 (2015) 2893–2939.
[21] K. Wu, Z. Chen, H. Lv, H. Zhu, C.L. Hill, T. Lian, J. Am. Chem. Soc. 136 (2014) 7708–7716.
[22] J. Chen, X.-J. Wu, L. Yin, B. Li, X. Hong, Z. Fan, B. Chen, C. Xue, H. Zhang, Angew. Chem. Int. Ed. 54 (2015) 1210–1214.
[23] A. Kudo, Y. Miseki, Chem. Soc. Rev. 38 (2009) 253–278.
[24] Z. Xie, X. Liu, W. Wang, X. Wang, C. Liu, Q. Xie, Z. Li, Z. Zhang, Nano Energy 11 (2015) 400–408.
[25] C. Han, Z. Chen, N. Zhang, J.C. Colmenares, Y.-J. Xu, Adv. Funct. Mater. 25 (2015) 221–229.
[26] W. Xu, C. Zheng, H. Hua, Q. Yang, L. Chen, Y. Xi, C. Hu, Appl. Surf. Sci. 327 (2015) 140–148.
[27] L. Wang, W. Wang, CrystEngComm 14 (2012) 3315–3320.
[28] T. Yan, L. Li, W. Tong, J. Zheng, Y. Wang, G. Li, J. Solid State Chem. 184 (2011) 357–364.
[29] R. Lacomba-Perales, J. Ruiz-Fuertes, D. Errandonea, D. Martínez-García, A. Segura, Europhys. Lett. 83 (2008), 37002-p1–37002-p5.
[30] Y. Abraham, N.A.W. Holzwarth, R.T. Williams, Phys. Rev. B 62 (2000) 1733–1741.
[31] Z.-F. Huang, J. Song, L. Pan, X. Zhang, L. Wang, J.-J. Zou, Adv. Mater. 27 (2015) 5309–5327.
[32] J. Song, Z.-F. Huang, L. Pan, J.-J. Zou, X. Zhang, L. Wang, ACS Catal. 5 (2015) 6594–6599.
[33] C. Guo, S. Yin, M. Yan, M. Kobayashi, M. Kakihana, T. Sato, Inorg. Chem. 51 (2012) 4763–4771.
[34] J.-J. Zou, H. He, L. Cui, H.-Y. Du, Int. J. Hydrogen Energy 32 (2007) 1762–1770.
[35] S. Wang, L. Pan, J.-J. Song, W. Mi, J.-J. Zou, L. Wang, et al., J. Am. Chem. Soc. 137 (2015) 2975–2983.
[36] A.J. Rondinone, M. Pawel, D. Travaglini, S. Mahurin, S. Dai, J. Colloid Interface Sci. 306 (2007) 281–284.
[37] N. Liu, C. Schneider, D. Freitag, U. Venkatesan, V.R.R. Marthala, M. Hartmann, B. Winter, E. Spiecker, A. Osvet, E.M. Zolnhofer, K. Meyer, T. Nakajima, X. Zhou, P. Schmuki, Angew. Chem. Int. Ed. 53 (2014) 14201–14205.
[38] S.A. Ivanov, A. Piryatinski, J. Nanda, S. Tretiak, K.R. Zavadil, W.O. Wallace, D. Werder, V.I. Klimov, J. Am. Chem. Soc. 129 (2007) 11708–11719.
[39] W. Tong, L. Li, W. Hu, T. Yan, G. Li, J. Phys. Chem. C 114 (2010) 1512–1519.
[40] R.J. Bose, R.V. Kumar, S.K. Sudheer, V.R. Reddy, V. Ganesan, V.P.M. Pillai, J. Appl. Phys. 112 (2012) 114311.
[41] Z.-F. Huang, J. Song, L. Pan, F. Lv, Q. Wang, J.-J. Zou, X. Zhang, L. Wang, Chem. Commun. 50 (2014) 10959–10962.
[42] Y. Hong, Y. Jiang, C. Li, W. Fan, X. Yan, M. Yan, W. Shi, Appl. Catal. B: Environ. 180 (2016) 663–673.